

# A nanoindentation study on grain-boundary contributions to strengthening and aging degradation mechanisms in advanced 12 Cr ferritic steel

Jae-il Jang

*Division of Materials Science and Engineering, Hanyang University, Seoul 133-791, Korea*

Sanghoon Shim

*Materials Science and Technology Division, Oak Ridge National Laboratory, Oak Ridge, Tennessee 37831; and Department of Materials Science and Engineering, The University of Tennessee, Knoxville, Tennessee 37996-2200*

Shin-ichi Komazaki<sup>a)</sup> and Tetsuya Honda

*Department of Materials Science and Engineering, Muroran Institute of Technology, Muroran 050-8585, Japan*

(Received 19 July 2006; accepted 25 September 2006)

Nanoindentation experiments and microstructural analysis were performed on advanced 12% Cr ferritic steel having extremely fine and complex martensitic microstructures, to answer unsolved questions on the contributions of grain boundaries to strengthening and aging degradation mechanisms in both as-tempered and thermally aged steels. Interesting features of the experimental results led us to suggest that among several high angle boundaries, block boundary is most effective in enhancing the macroscopic strength in as-tempered virgin sample, and that a decrease in matrix strength rather than reduction in grain-boundary strengthening effect is primarily responsible for the macroscopic softening behavior observed during thermal exposure.

## I. INTRODUCTION

To meet the demand for efficiency improvement in fossil power plants by elevating steam temperature and pressure, some advanced heat-resistant steels have been developed with excellent mechanical performance under such severe conditions. Recently, advanced high (9–12%) Cr ferritic/martensitic steels have received increasing attention as strong candidates for the heat-resistant materials in the ultra-super-critical (USC) power plants thanks to their superior high-temperature strengths (especially creep strength) as well as superior oxidation and corrosion resistance to conventional high Cr steels.<sup>1</sup>

These advanced high Cr ferritic/martensitic steels generally have extremely fine and complex lath-martensitic microstructures, and the excellent strengths of the steels might be attributed to the combined strengthening mechanisms of the matrix and grain boundaries, as in many other martensitic steels.<sup>2</sup> Figure 1 schematically illustrates the microstructural parameters possibly affecting the strengthening mechanisms of advanced 12% Cr

steels. First, the matrix strength can be enhanced by intrinsic strain hardening (due to high dislocation density), solid-solution strengthening (by W and Mo), and particle strengthening (by  $M_{23}C_6$ , MX, and Laves phases). Second, grain-boundary strengthening will additionally elevate the macroscopic strength of the steels. Note that the grain-boundary strengthening discussed here is limited to conventional dislocation-based polycrystalline strengthening concept that induces Hall-Petch relation,<sup>3</sup> and does not include the role of grain boundaries as sources of other strengthening mechanisms (e.g., as heterogeneous nucleation sites for precipitates that induce particle strengthening). As shown in Fig. 1, the steels contain several boundaries dividing the microstructures into different units: (i) extremely fine lath, (ii) block subdivided into laths, (iii) packet made up of several blocks, and (iv) prior-austenite grain (the largest unit). Of these boundaries, the lath boundary is a small-angle boundary and the rest are high-angle ones.<sup>4–6</sup>

While many studies have been made on the detailed matrix strengthening mechanisms in advanced high Cr steels (as well reviewed in Ref. 1), the contributions of the boundaries to the macroscopic mechanical response have not been clearly understood but are expected to be significant. This is simply because it is difficult to isolate the contributions of the boundaries mainly due to the fine

<sup>a)</sup>Address all correspondence to this author.  
e-mail: komazaki@mmm.muroran-it.ac.jp  
DOI: 10.1557/JMR.2007.0009

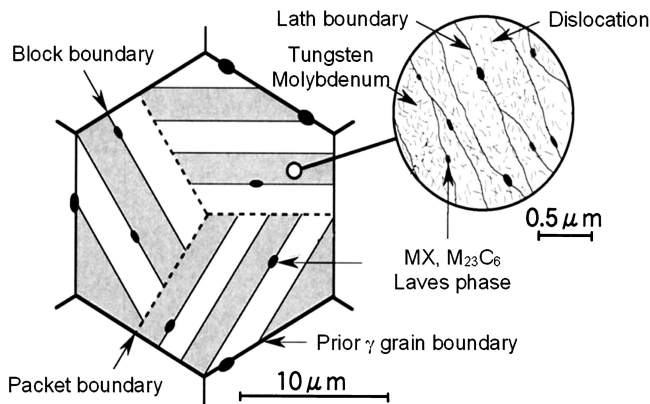


FIG. 1. Schematic illustration of the complex microstructural parameters affecting strengthening mechanisms in the advanced 12% Cr steel examined here.

and complex microstructures. One possible way to directly measure the individual strength characteristics of complex microstructures with submicron dimensions is nanoindentation, which can evaluate hardness of such small volumes merely by analyzing the indentation load-displacement ( $P$ - $h$ ) curve.<sup>7,8</sup> Recently, pioneering works in applying the nanoindentation technique to strength analysis of martensitic steels have been performed by Ohmura and colleagues,<sup>9–12</sup> who suggested that the matrix strength of Fe-C binary martensitic steels can be successfully measured by nanoindentation (performed mainly at 0.5 mN) without the contribution of high-angle boundaries. From a similar viewpoint, Sawada et al.<sup>13</sup> have very recently reported the correlation between microstructures and nano-/micro-hardness in modified 9Cr-1Mo steel.

In this work, we performed a series of nanoindentation experiments on an advanced 12% Cr steel (which has been used in steam turbine rotors of commercial power plants) to identify the grain-boundary contributions to the mechanical response of this steel. The analysis here focuses on two objectives: (i) to determine which boundary is the most effective in elevating the macroscopic strength of the virgin steel, and (ii) to examine the contribution of the boundaries to macroscopic strength degradation during thermal aging.

## II. EXPERIMENTAL PROCEDURE

### A. Material

The material examined in this study is an advanced 12%Cr ferritic steel whose chemical composition in addition to Fe is 10.02Cr-0.99Mo-0.19V-1.00W-0.14C-0.05Nb-0.0373N-0.04Si-0.62Mn-0.007P-0.0025S-0.70Ni (mass%). This commercial-grade steel is typically processed by normalizing and tempering treatments for turbine rotor applications. In this work, the as-tempered virgin samples were thermally aged under three

specific conditions; at 903 K for 3000 h, at 923 K for 3000 h, and at 923 K for 16000 h. Throughout this article, the degree of thermal aging will be described as a Larson-Miller parameter (LMP), which is given by

$$\text{LMP} = T(C + \log t) \times 10^{-3} \quad (1)$$

where  $T$  and  $t$  are the aging temperature and time in the units of K and h, respectively, and  $C$  is the Larson-Miller constant (taken here as 36; this value is known to be appropriate for arranging creep-rupture test results for high Cr steels).<sup>14,15</sup>

### B. Nanoindentation

Nanoindentation experiments were carried out using a Nanoindenter-XP (MTS Corp., Oak Ridge, TN) with a typical three-sided pyramidal Berkovich indenter tip. The maximum indentation load ( $P_{\max}$ ) was varied (0.5, 1, 5, 10, 50, 100, 400, and 700 mN), and the tip calibration and hardness calculation were conducted in accordance with the Oliver-Pharr method.<sup>7</sup> To measure macroscopic strength change during thermal exposure, Vickers hardness tests were preliminarily conducted at  $P_{\max} = 9.8$  N. More than five indentation tests under each testing condition were made on electro-polished samples instead of mechanically polished samples, to avoid artifacts related to a hardened surface layer. The specimen surfaces were initially ground with fine emery paper of #2400 and then electrically polished in a phosphoric acid solution (100 ml) with chromium oxide VI (50 g) at a temperature of 348 K and current density of 0.8 mA/mm<sup>2</sup> for 60 s.

### C. Microstructure observations

The microstructural features were examined by optical microscopy and transmission electron microscopy (TEM). Thin foils for TEM observation were prepared using conventional twin-jet electropolishing in a solution of 10% perchloric acid and 90% methanol at a temperature of 213–223 K and a potential of 10–20 V. TEM observations were performed using a JEM-200CX (Japan Electron Microscope, Japan) at 200 kV. To get information about the sizes and compositions of precipitates, an extraction replica technique was applied through a TEM equipped with the energy dispersive x-ray spectroscopy (EDX). Precipitates were electrolytically extracted as residue from each sample using a 10% acetyl acetone and 1% tetramethyl ammonium chloride-methanol electrolyte. The weights of the extracted residues were measured by microbalance. The amounts of  $M_{23}C_6$  carbide and Laves phase were determined separately according to the procedure of Kutsumi et al.<sup>16</sup>: chemical dissolution of the Laves phase in 1% bromine-methanol at 323 K for 1.5 h and subsequent weighing of the remaining residue ( $M_{23}C_6$  carbide).

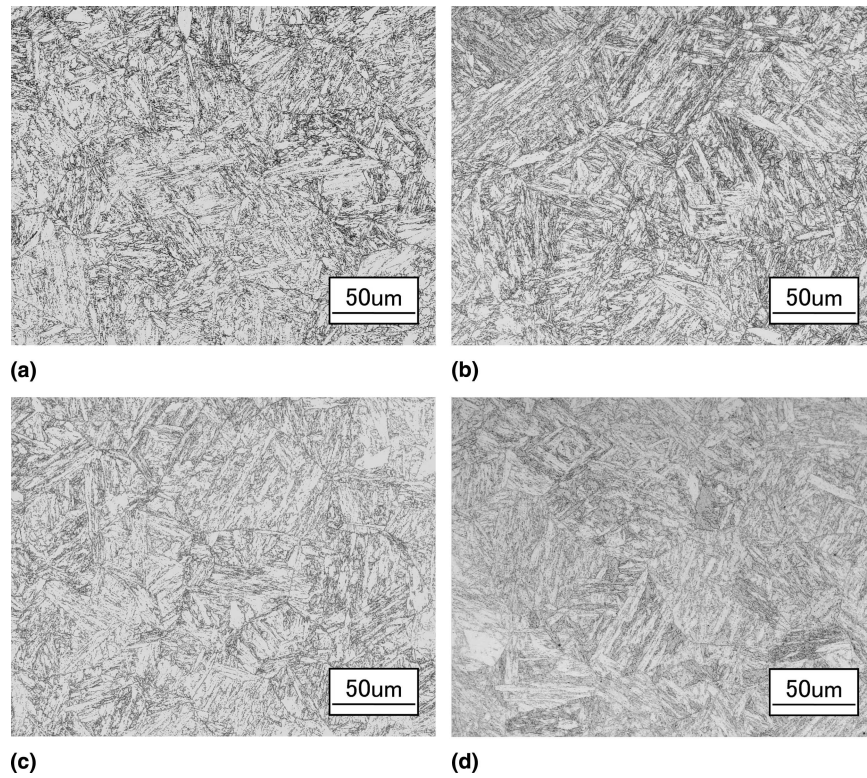


FIG. 2. Optical micrographs of the as-tempered virgin sample and the aged samples: (a) as-tempered, and aged (b) at 903 K for 3000 h, (c) at 923 K for 3000 h, and (d) at 923 K for 16000 h.

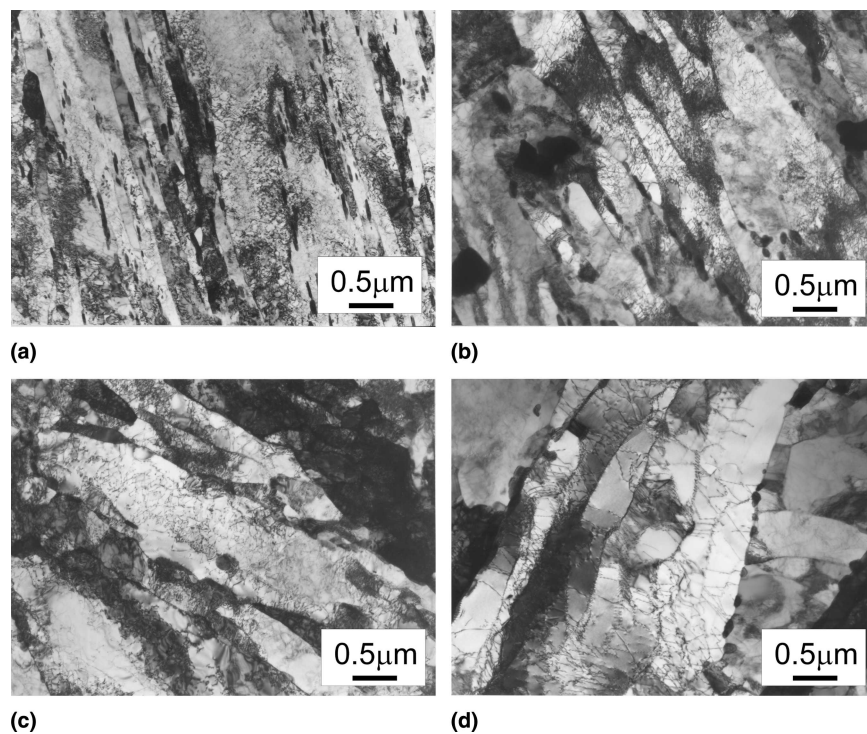


FIG. 3. Bright-field TEM micrographs of the as-tempered virgin sample and the aged samples: (a) as-tempered, and aged (b) at 903 K for 3000 h, (c) at 923 K for 3000 h, and (d) at 923 K for 16000 h.

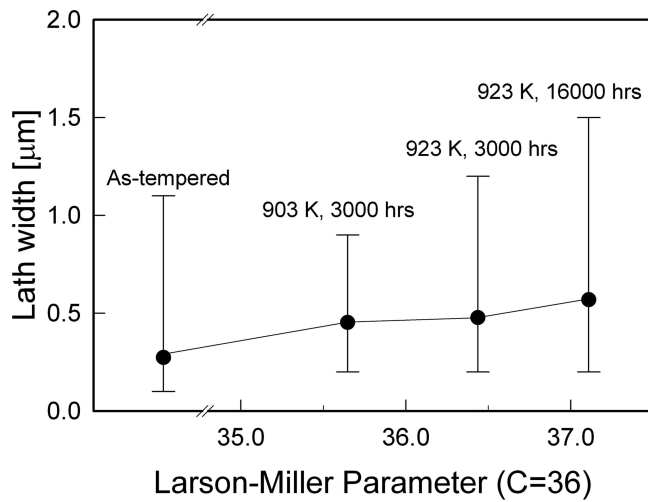


FIG. 4. Change in lath width with increasing degree of thermal aging (LMP). The solid circle indicates the average value.

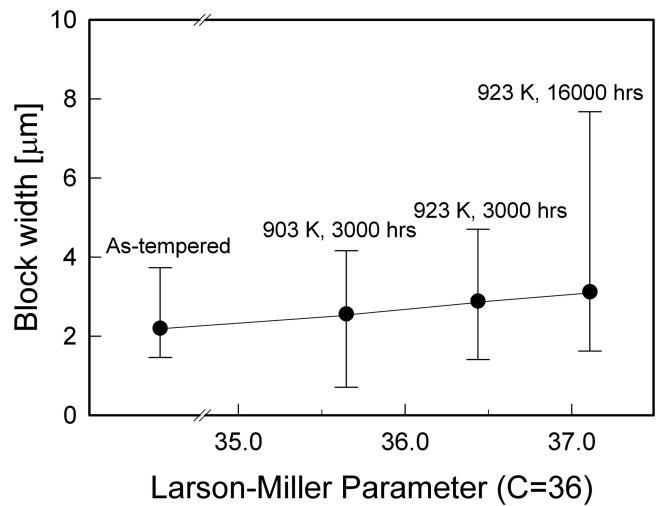
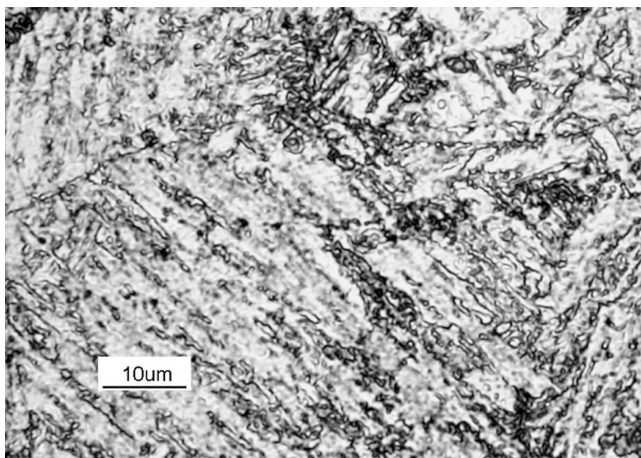
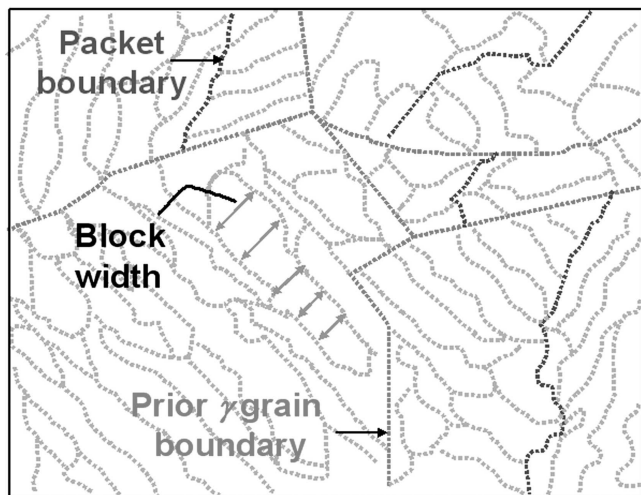


FIG. 6. Change in block size during thermal exposure. The solid circle indicates the average value.



(a)



(b)

FIG. 5. An example of simple grain-boundary mapping to determine block size: (a) optical micrograph and (b) resulting grain-boundary map.

### III. RESULTS

#### A. Sizes of microstructural units

Optical micrographs of the as-tempered and aged samples are shown in Fig. 2. All samples have a typical tempered lath-martensitic structure without any delta ferrite, and the microstructures in optical microscopic resolution are not altered noticeably by thermal aging. The size of the prior austenite grain in as-tempered virgin sample was greater than 50  $\mu\text{m}$ , and no obvious change was detected with aging.

Figure 3 exhibits bright-field TEM micrographs of the as-tempered and aged samples. The microstructure consists of several martensite laths containing high density of dislocations, which might be produced by the martensitic transformation during normalizing. The lath width in as-tempered sample was around 0.2 ~ 0.5  $\mu\text{m}$ , in good agreement with the value previously reported.<sup>17,18</sup> As thermal aging progressed, the lath width clearly increased, as shown in Fig. 3. The width change was measured from more than 10 TEM images for each sample, and the results are summarized as a plot of lath width versus LMP in Fig. 4. The solid circle in the figure indicates the average value whereas the maximum and minimum values are marked by the uncertainty bars. Although the values obtained were widely distributed depending on location, a trend of average lath width to increase with increasing LMP is visible. It is noteworthy that the uncertainty bar for as-tempered sample is very large because somewhat large laths were observed in a few images although most observations indicated very small lath widths.

While the sizes of prior austenite grain and lath could be measured simply by using the optical microscopy and TEM images respectively, it was relatively difficult to determine the block size, and unfortunately we could not

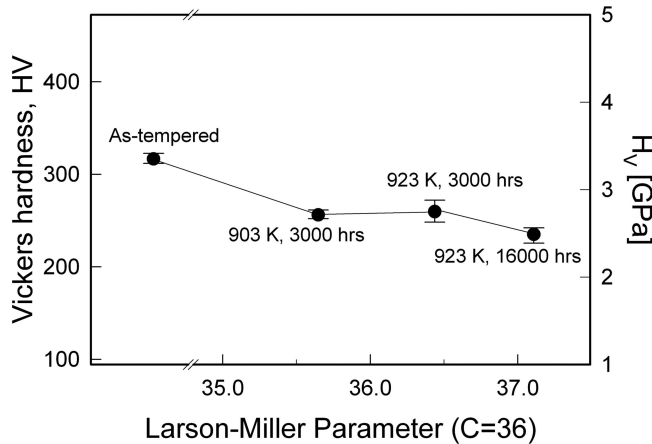


FIG. 7. Change in Vickers hardness with thermal aging. The solid circle indicates the average value.

critically judge the size of packets in this study. To determine the block width, we performed more severe etching than used for Fig. 2, and measured the widths of more than 30 blocks by grain-boundary mapping (e.g., Fig. 5). The change in block size with LMP is described in Fig. 6. The average block width in as-tempered samples is approximately 2 ~ 3 μm (consistent with the value recently reported by Kimura et al.),<sup>19</sup> and the block width gradually increases with LMP.

**B. Hardness**

Figure 7 shows the results of preliminary Vickers hardness tests to measure macroscopic strength changes during thermal aging. For direct relation to the nanoindentation hardness ( $H_n$ ), the conventional Vickers hardness HV (defined as the maximum indentation load divided by the “surface area” of indentation  $A_S$ ) must be converted to indentation hardness,  $H_V$  which is equal to mean contact pressure under the indenter (i.e., the peak load divided by the “projected area” of indentation  $A_P$ ). The conversion process is simply given as

$$\begin{aligned}
 HV &= \frac{P_{max}}{A_S} = \frac{2 \sin 68^\circ P_{max}}{d^2} = \left( \frac{P_{max}}{A_P} \right) \sin 68^\circ \\
 &= H_V \sin 68^\circ \quad , \quad (2)
 \end{aligned}$$

where  $P_{max}$  is the peak load and  $d$  is the Vickers indentation diagonal. It is apparent from Fig. 7 that the Vickers hardness value ( $H_V$  or HV) tends to decrease during thermal exposure. The maximum and the minimum values of averaged hardness, 3.3 GPa (HV317) and 2.5 GPa (HV235), were obtained from the as-tempered sample and the sample aged at 923 K for 16000 h respectively, whereas the other two samples, aged at 903 K and at 923 K respectively for the same time of 3000 h, showed similar hardness values (about 2.7 GPa).

Typical nanoindentation load-displacement (P-h)

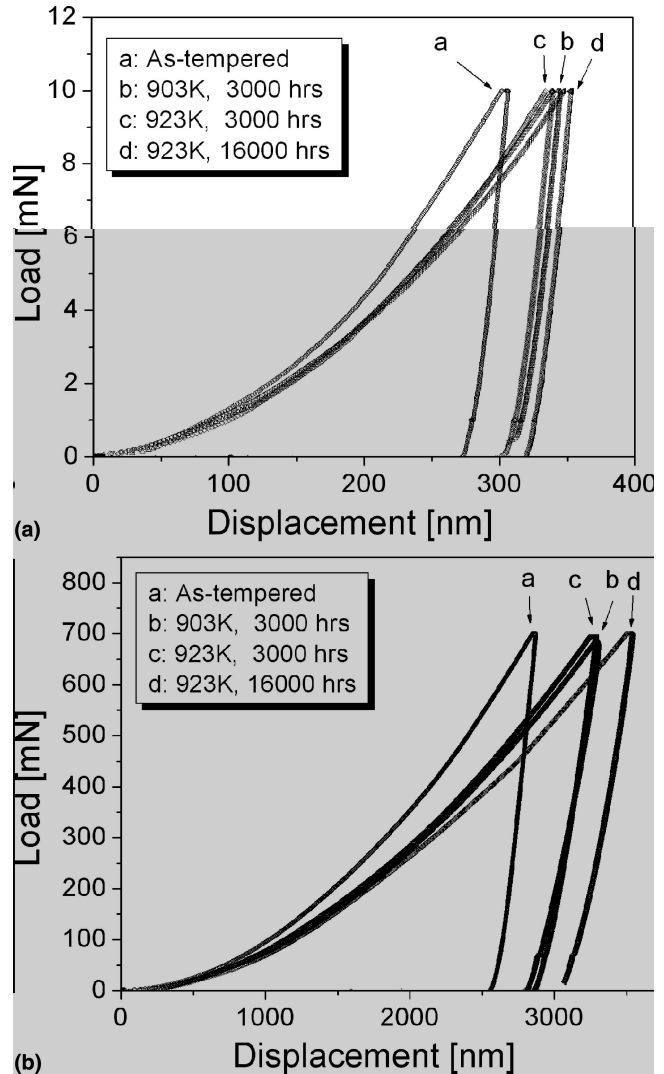


FIG. 8. Variations in nanoindentation load-displacement curves according to thermal aging condition: (a)  $P_{max} = 10$  mN, (b)  $P_{max} = 700$  mN.

curves obtained at relatively low load ( $P_{max} = 10$  mN) and high load ( $P_{max} = 700$  mN) are illustrated in Fig. 8. In both cases, the as-tempered sample exhibits the smallest displacement at given  $P_{max}$  (which means the highest hardness), while the sample aged for 16000 h shows the lowest hardness. Figure 9 summarizes the results of nanoindentation experiments performed at different levels of  $P_{max}$  from 0.5 mN to 700 mN (the maximum load capacity of the instrument used here). The wide fluctuation in nanoindentation hardness ( $H_n$ ) seen in the figure might arise from intrinsic microstructural inhomogeneity (involving the amount of precipitates and solid-solution elements) in the indented locations. Nevertheless, the nanoindentation experiments at every load level showed tendencies of  $H_n$  change with LMP very similar to the trend of  $H_V$  change in Fig. 7. A somewhat surprising feature illustrated in Fig. 9 is the opposite tendency of  $H_n$

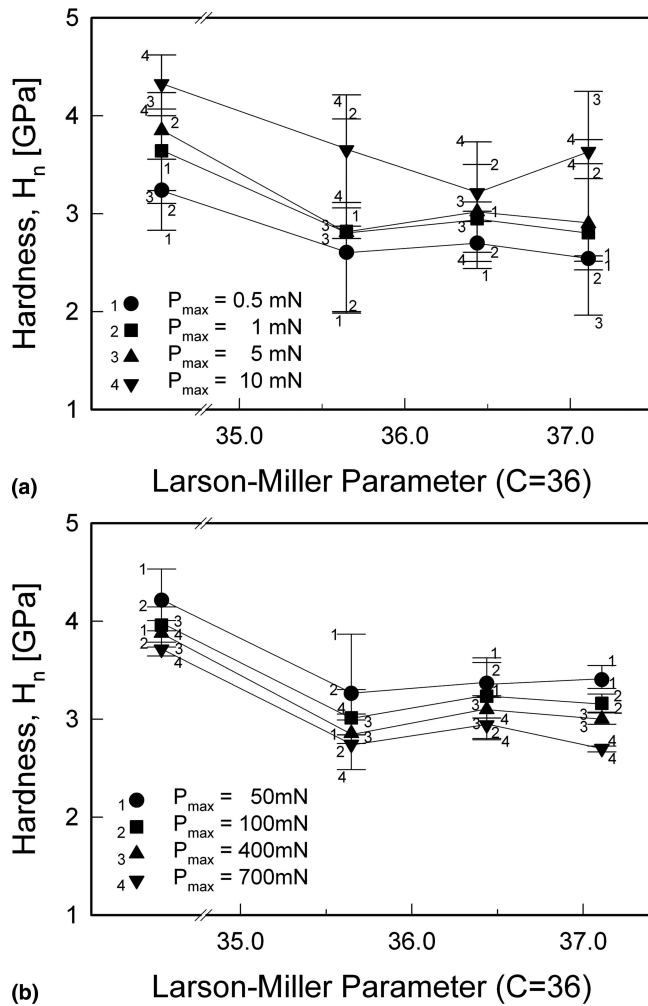


FIG. 9. Summary of  $H_n$  variation during thermal aging: (a) relatively low-load indentations ( $P_{max} = 0.5\text{--}10$  mN), and (b) high-load indentations ( $P_{max} = 50\text{--}700$  mN). The solid symbols (circle, square, and triangle) indicate the average value.

variation with  $P_{max}$  observed at different load levels: for a given LMP,  $H_n$  increases with increasing  $P_{max}$  in the relatively low-load regime [Fig. 9(a)], but the opposite trend was observed in the high-load regime [Fig. 9(b)]. This interesting observation may present a clue to the grain-boundary contribution to the strengthening mechanism, as discussed in Sec. IV.

#### IV. DISCUSSION

##### A. Strengthening in as-tempered virgin steel

In Fig. 9, for a given LMP, the tendency of variation in  $H_n$  with  $P_{max}$  can be roughly divided into two parts: the relatively high-load regime and the low-load regime. In the high-load regime [Fig. 9(b)],  $H_n$  decreases as  $P_{max}$  increases, which might be simply explained by the well-known “the smaller, the harder” concept of indentation size effect (ISE).<sup>20,21</sup> Since Vickers hardness values ( $H_V$ )

obtained at 9.8 N (see Fig. 7) are smaller than  $H_n$  measured at 700 mN, one might expect the decreasing trend of hardness with increasing  $P_{max}$  to be maintained at macro-indentation load levels.

In contrast, in the low-load regime [Fig. 9(a)],  $H_n$  was found to increase as  $P_{max}$  increased. This is curious because it is directly opposite to the concept of ISE. The trend is more clearly seen in Fig. 10, which shows the result from the as-tempered sample separately. The “inverse-ISE behavior” (the increase in hardness with increasing depth or  $P_{max}$ ) is maintained up to  $h_{max} \sim 300$  nm (Figs. 8 and 10), and thus the behavior is not related to tip-blunting effect but to the complex nature of the microstructures in this steel.

Working from the above interesting observation, an important insight into the grain-boundary contribution to strengthening mechanisms in as-tempered virgin steel was gained by comparing the size of each microstructure unit (which means grain-boundary spacing) to the size of the indentation-induced plastic zone. According to Johnson’s expanding-cavity model for elastic-plastic indentation with a cone,<sup>22</sup> one may estimate the plastic zone radius,  $r_p$ , as

$$r_p = a \left\{ \frac{1}{6(1-\nu)} \left[ \frac{E}{\sigma_{YS}} \tan \beta + 4(1-2\nu) \right] \right\}^{1/3}, \quad (3)$$

where  $a$  is contact radius,  $\beta$  is the angle of inclination of the conical indenter to the surface of the edge of indentation,  $E$  is Young’s modulus,  $\nu$  is Poisson’s ratio, and  $\sigma_{YS}$  is the yield strength. To relate this conical indentation model to the present results, we make the usual assumption that similar behavior is obtained when the angle of the cone gives the same area-to-depth relation as

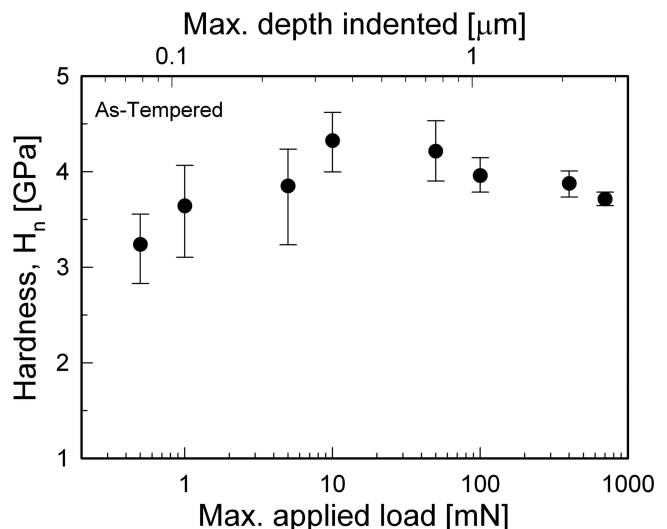


FIG. 10. Variation in  $H_n$  with increasing indentation load (and displacement) in as-tempered virgin sample. The solid circle indicates the average value.

the pyramid. For the Berkovich indenter (whose center-line-to-face angle is  $65.3^\circ$ ), the equivalent cone angle is  $70.3^\circ$  and thus  $\beta$  is  $19.7^\circ$ . Accordingly, by putting  $E = 200$  GPa,  $\sigma_{YS} = 710$  MPa (measured by tensile tests of similar steel),<sup>23</sup>  $\nu = 0.3$ , and the contact radius (determined by the Oliver-Pharr method)<sup>7</sup> into the right-hand term of Eq. (3), we could estimate the plastic zone size. Note that the shape of the plastic zone is assumed as a hemisphere according to Johnson's model.<sup>22</sup> The average values of the estimated plastic zone "diameter" are given as a function of  $P_{max}$  in Fig. 11. For as-tempered sample, the estimated value was approximately  $1.2 \mu\text{m}$  for  $P_{max} = 0.5$  mN,  $1.6 \mu\text{m}$  for 1 mN,  $3.6 \mu\text{m}$  for 5 mN,  $5.0 \mu\text{m}$  for 10 mN,  $11.2 \mu\text{m}$  for 50 mN,  $16.4 \mu\text{m}$  for 100 mN,  $33.2 \mu\text{m}$  for 400 mN, and  $45.0 \mu\text{m}$  for 700 mN.

At  $P_{max} = 0.5$  mN, the calculated diameter of the hemispherical plastic zone in the as-tempered sample is around  $1.2 \mu\text{m}$ , which is greater than the lath width but less than the averaged block width. Therefore, at such a low load, the plastic zone may include only lath boundaries. Since a lath boundary is a low-angle boundary, one might consider that a block (consisting of several laths) is essentially a single crystal of martensite.<sup>6</sup> Thus, it seems reasonable to assume that the obtained hardness is the matrix strength of this virgin sample. At  $P_{max} = 1$  mN, the diameter of the plastic zone (about  $1.6 \mu\text{m}$ ) is still a little below the average block width ( $2\text{--}3 \mu\text{m}$ ). However, the possibility that the material under indenter has a block boundary within its plastic zone is greater than that at  $P_{max} = 0.5$  mN. Thus, hardness could increase due to the possible block boundary strengthening effect. At  $P_{max} = 5$  mN, the plastic zone diameter is about  $3.6 \mu\text{m}$ , and the material under the indenter should meet one or two block boundaries; thus the influences of block boundary strengthening (and resulting hardness value) are greater than at  $P_{max} = 1$  mN. When  $P_{max}$  increases to

10 mN, the plastic zone diameter is around  $5.0 \mu\text{m}$ . Although this is still below the packet size (which is known to be much greater than the block size) and prior austenite grain size, it might be large enough to have significant block boundary strengthening effects. In the higher-load regime ( $P_{max} > 10$  mN in Fig. 10),  $H_n$  decreases with increasing  $P_{max}$ , even though the plastic zone sizes are larger than at  $P_{max} = 10$  mN. The transition from inverse-ISE to ISE was more evident in continuous hardness measurement using the continuous stiffness measurement (CSM) technique,<sup>7,8</sup> as shown in Fig. 12. It should be noted that the principle of 'the smaller, the harder' is valid only if there is no significant change in microstructural environment sampled. Thus the above results may imply that (i) despite the different size, the plastic zones formed during indentations at 10 mN and 700 mN (and possibly at 9.8 N) have similar microstructural environments (but different size), and thus that (ii) the plastic zone at  $P_{max} = 10$  mN is already big enough to reflect the major grain-boundary strengthening effect that seems to arise from block boundaries. We emphasize that, if the boundaries of packets or prior austenite grains rather than blocks play important roles in strengthening this virgin sample, the inverse-ISE behavior should be observable at much higher load levels than 10 mN. Therefore, it is possible to conclude that the boundaries of packet and prior austenite grain are much less effective in strengthening this material than block boundaries. This might be related with much higher density of block boundary within the plastic zone than those of other high-angle boundaries. Collectively, from the viewpoint of grain-boundary strengthening, the block size is indeed the effective grain size of this steel, which means that macroscopic strength of this steel is definitely enhanced by the block boundaries rather than other high-angle boundaries.

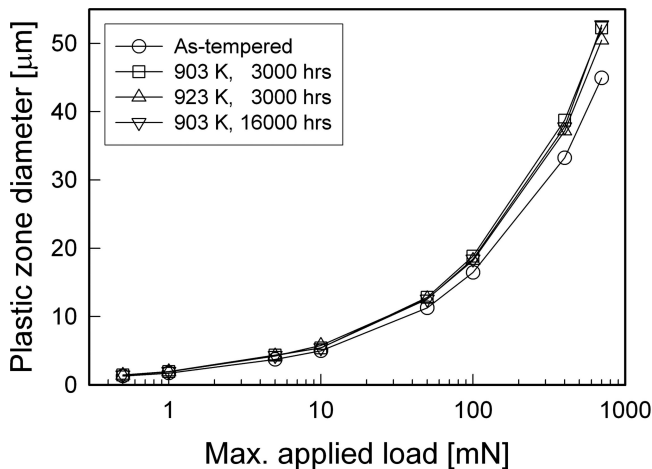


FIG. 11. Calculated plastic zone size as a function of maximum indentation load  $P_{max}$ .

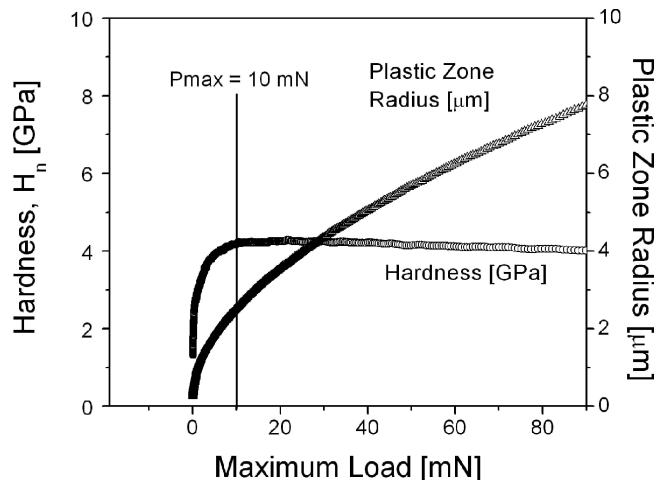


FIG. 12. CSM-mode nanoindentation result showing variations in both hardness and plastic zone radius with maximum indentation load,  $P_{max}$ .

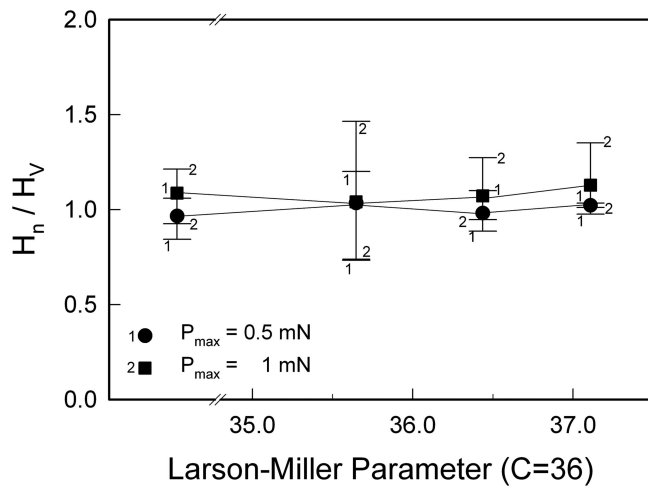


FIG. 13. Variations in  $H_n/H_V$  ratio with increasing LMP. The  $H_n$  values were obtained from nanoindentations made at low loads ( $P_{max} = 0.5$  and  $1$  mN). The solid circle and square indicate the average value.

### B. Softening during thermal aging

Like many other Cr-Mo-based heat-resistant steels, the advanced 12% Cr steel examined here underwent macroscopic strength degradation during thermal aging (Fig. 7). Because the macroscopic strength like Vickers hardness ( $H_V$ ) is determined by contributions of both the matrix and grain boundaries, as discussed previously, it

is constructive to consider which contribution plays the main role in the macroscopic strength degradation.

In a manner similar to the analysis in the previous section, one might speculate that if grain-boundary strengthening effects are significant in the aging degradation mechanism, the tendency of  $H_n$  change with LMP should be clearly dependent on the indentation-induced plastic zone size (and thus  $P_{max}$ ); i.e., the tendency detected in low-load nanoindentation should be different from that in high-load nanoindentation or Vickers indentation. However, as shown in Fig. 9, the trends observed during nanoindentation experiments are almost independent of  $P_{max}$ . Recently, Ohmura et al.<sup>9</sup> suggested that if the nanoindentation load is very small (such as  $0.5$  mN in their study), the ratio of nanoindentation hardness to macrohardness is closely associated with the degree of contribution of the matrix strength to the macroscopic strength. That is, if the grain-boundary strengthening effect is larger, the ratio is smaller. Similarly, we examined the dependence of the ratio of  $H_n/H_V$  on LMP, as seen in Fig. 13. For nanoindentations made at  $0.5$  mN and  $1$  mN, respectively (which may provide only matrix strengths because most of the high-angle boundaries are not sampled at these low loads), the  $H_n/H_V$  ratio does not vary significantly with LMP and remains approximately constant. In addition, because the value of the  $H_n/H_V$  ratio in Fig. 13 is close to unity, it is predictable that the contribution of matrix strength to macroscopic strength is conceivably much

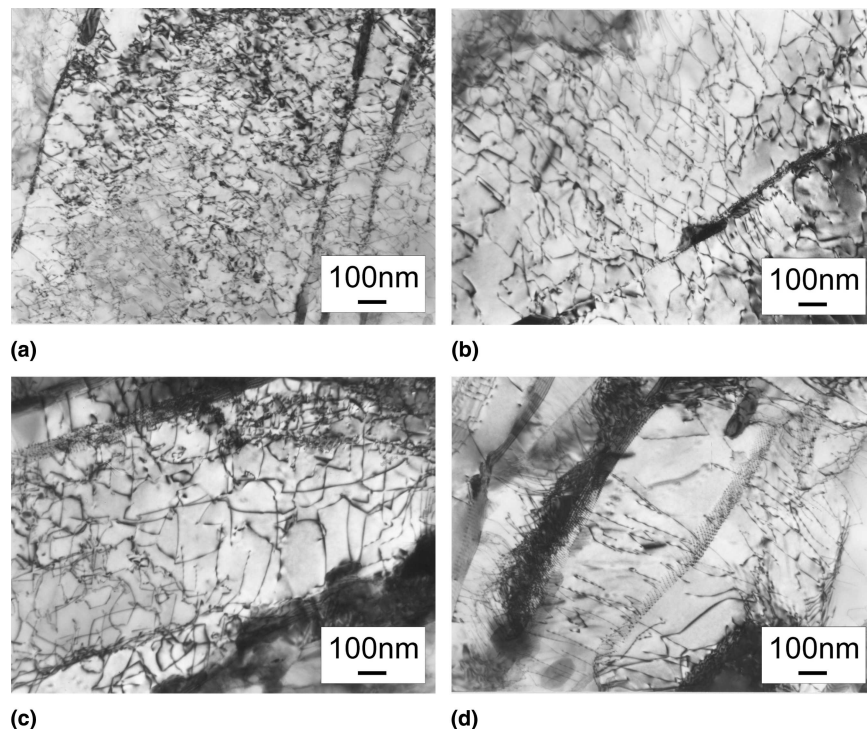


FIG. 14. TEM micrographs showing dislocation structures inside martensite lath: (a) as-tempered virgin sample, and samples aged (b) at  $903$  K for  $3000$  h, (c) at  $923$  K for  $3000$  h, and (d) at  $923$  K for  $16000$  h.

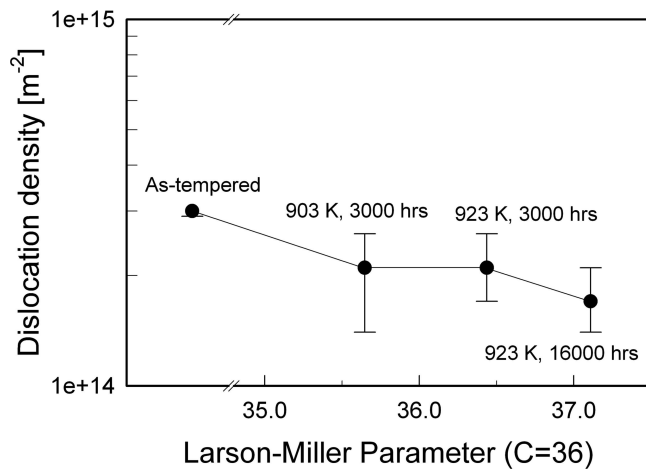


FIG. 15. Change in dislocation density during thermal aging. The solid circle indicates the average value.

higher than that of high-angle-boundary-enhanced strength. All of these results led us to suggest that in this steel, the decrease in matrix strength is primarily responsible for the macroscopic strength degradation during thermal exposure. However, it should be also noted that due to the indentation size effect (ISE), it is hard to directly compare the  $H_n$  (obtained at 0.5 mN or 1 mN) to the  $H_v$  (at 9.8 N); i.e., the real ratio of matrix strength to

macroscopic overall strength should be smaller than unity (as we discussed in Sec. IV. A). Thus there can be a small contribution of the decrease in high-angle-boundary-strengthening effect to the macroscopic aging degradation, which might be explained by the increase in the block width with aging (Fig. 6).

Since macroscopic softening during thermal aging seems to be mainly due to the degradation in matrix strength rather than the reduction of high-angle-boundary strengthening effect, we additionally examined microstructural parameters affecting the matrix strength (Fig. 1) and their variations with LMP to explain the major mechanism of the degradation phenomena.

(i) It is well accepted that the high strength of martensite matrix is basically caused by its high dislocation density. Typical dislocation structures inside lath of as-tempered and aged samples are shown in Fig. 14. The density was measured using more than 10 TEM images for each sample, and the results are summarized in Fig. 15. Although the values obtained were widely distributed depending on the location of the observation, Figs. 14 and 15 show that dislocation density decreases with increasing LMP.

(ii) Another well-known matrix-strengthening mechanism is particle strengthening such as precipitation hardening and dispersion hardening. Figure 16, representing

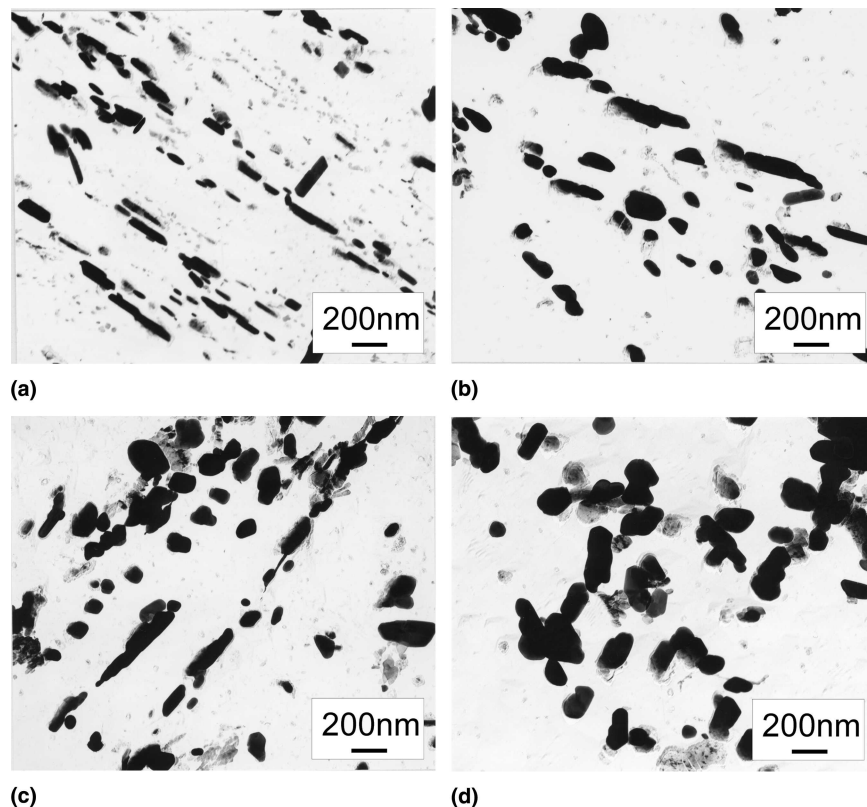


FIG. 16. TEM micrographs of extracted replicas of the as-tempered and aged samples: (a) as-tempered, and aged (b) at 903 K for 3000 h, (c) at 923 K for 3000 h, and (d) at 923 K for 16000 h.

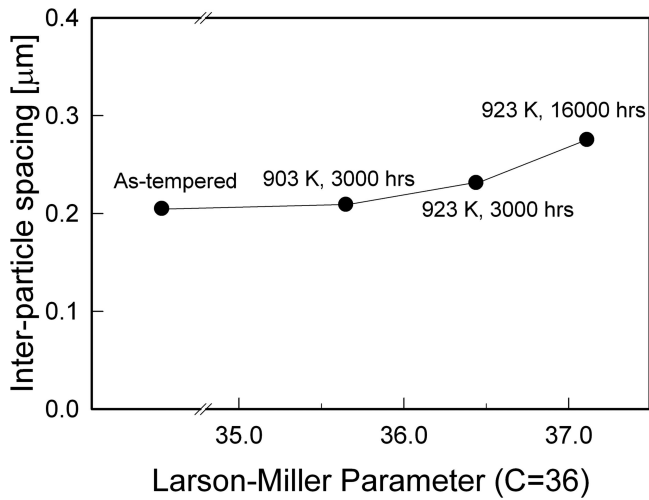


FIG. 17. Variation in calculated inter-particle spacing according to thermal aging.

TEM micrographs of the extracted replica samples, demonstrates that the precipitate size increases as LMP increases, and that very coarse precipitates (as large as 1  $\mu\text{m}$ ) were often observed in the most aged sample. Subsequent EDX analysis revealed that the majority of the massive particles were  $\text{M}_{23}\text{C}_6$ -type carbides. While Laves phase  $[(\text{Fe},\text{Cr})_2(\text{Mo},\text{W})]$  was identified only in the aged steels, some extremely fine CrN (with a size of 10 nm) was observed solely in the lath interior of the as-tempered sample. Throughout the aging process, the amount of Laves phase (which did not exist in the as-tempered sample) increased but the amount of  $\text{M}_{23}\text{C}_6$  carbide remained almost constant, implying that the precipitation of  $\text{M}_{23}\text{C}_6$  carbide was already complete during the normalizing and tempering treatments of the virgin sample. The inter-particle spacing, which is the most

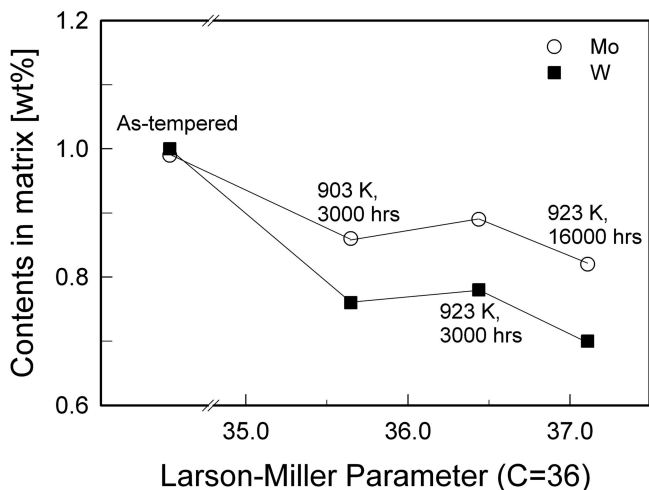


FIG. 18. Changes in calculated amounts of Mo and W elements according to thermal aging.

important factor in particle strengthening,<sup>3</sup> was calculated based on the average value of precipitate amounts (measured using TEM images like Fig. 16), as shown in Fig. 17. The spacing gradually increases during thermal exposure from about 0.2  $\mu\text{m}$  in as-tempered sample to 0.3  $\mu\text{m}$  in the most aged sample.

(iii) The amounts of W and Mo (both of which are known to induce significant solid-solution strengthening in advanced 12% Cr steels)<sup>1</sup> were calculated from the average value of measured precipitate amounts for each sample and are plotted as a function of LMP in Fig. 18. The amounts of Mo and W quickly decrease at early stages of aging, corresponding to the precipitation of Laves phase. Since Laves phase contains more W than Mo, the reduction in W content with aging is more pronounced.

(iv) Finally, the increase in lath width with aging (Fig. 4) can be included among the possible microstructural changes responsible for the matrix strength degradation, if a martensite block is considered as a single crystal martensite as a lath boundary is small-angle boundary.<sup>6</sup>

Since all these microstructural variations (i.e., decreases in dislocation density and solid-solution amounts, and increases in inter-particle spacing and lath width) are consistent with the tendency of degradation in matrix strength, it is still difficult to identify the predominant microstructural parameter governing the degradation in matrix strength and thus in macroscopic strength. One might imagine that the change in dislocation density is most critical to the degradation simply because the samples aged at 903 K and at 923 K for the same time of 3000 h exhibited very similar average  $H_V$  as well as average dislocation density. However, there are still large fluctuations in the data and the microstructural parameters may affect one another, and thus it would be unwise to draw such a simple conclusion. More systematic investigations of microstructural changes and their interactions are desirable to determine quantitatively the critical sources of matrix strength degradation.

## V. CONCLUSIONS

The contributions of grain boundaries to strengthening and aging degradation in an advanced 12% Cr ferritic/martensitic steel are investigated by nanoindentation experiments together with microstructural observations. The results presented here lead us to conclude that, among several high-angle boundaries, the block boundary is the most effective in enhancing the macroscopic strength of as-tempered virgin samples. It is also clear that high-angle boundaries may not be an important source of the thermal-aging-induced softening of this steel, and thus that a decrease in matrix strength may be

primarily responsible for the macroscopic strength degradation during thermal exposure.

## ACKNOWLEDGMENTS

A portion of this research was conducted at the SHaRE (SHared Research Equipment) User Facility, which is sponsored at Oak Ridge National Laboratory by the Division of Scientific User Facilities, U.S. Department of Energy. The authors thank Dr. Takayuki Sugimoto for technical assistance and Toshiba Corporation for providing the steel examined in this work.

## REFERENCES

1. R.L. Klueh: Elevated temperature ferritic and martensitic steels and their application to future nuclear reactors. *Int. Mater. Rev.* **50**, 287 (2005).
2. G. Krauss: Martensite in steel: Strength and structure. *Mater. Sci. Eng., A* **273–275**, 40 (1999).
3. G.E. Dieter: Mechanical Metallurgy (McGraw-Hill, UK, 1988) p. 184.
4. J.M. Marder and A.R. Marder: The morphology of iron-nickel massive martensite. *Trans. ASM* **62**, 1 (1969).
5. T. Maki, K. Tsuzaki, and I. Tamura: The morphology of microstructure composed of lath martensites in steels. *Trans. ISIJ* **20**, 207 (1980).
6. J.W. Morris, Jr., Z. Guo, C.R. Krenn, and Y-H. Kim: The limits of strength and toughness in steel. *ISIJ Int.* **41**, 599 (2001).
7. W.C. Oliver and G.M. Pharr: An improved technique for determining hardness and elastic modulus using load and displacement sensing indentation experiments. *J. Mater. Res.* **7**, 1564 (1992).
8. W.C. Oliver and G.M. Pharr: Measurement of hardness and elastic modulus by instrumented indentation: Advances in understanding and refinements to methodology. *J. Mater. Res.* **19**, 3 (2004).
9. T. Ohmura, K. Tsuzaki, and S. Matsuoka: Nanohardness measurement of high-purity Fe-C martensite. *Scripta Mater.* **45**, 889 (2001).
10. T. Ohmura, T. Hara, and K. Tsuzaki: Relationship between nano-hardness and microstructures in high-purity Fe-C as-quenched and quench-tempered martensite. *J. Mater. Res.* **18**, 1465 (2003).
11. T. Ohmura, T. Hara, and K. Tsuzaki: Evaluation of temper softening behavior of Fe-C binary martensitic steels by nanoindentation. *Scripta Mater.* **49**, 1157 (2003).
12. J. Li, T. Ohmura, and K. Tszuzaki: Evaluation of grain boundary effect on strength of Fe-C low alloy martensitic steels by nanoindentation technique. *Mater. Trans.* **46**, 1301 (2005).
13. K. Sawada, K. Miyahara, H. Kushima, K. Kimura, and S. Matsuoka: Contribution of microstructural factors to hardness change during creep exposure in mod. 9Cr-1Mo steel. *ISIJ Int.* **45**, 1934 (2005).
14. F. Masuyama and N. Komai: Long-term creep rupture strength of tungsten-strengthened advanced 9–12% Cr steels. *Key Eng. Mater.* **171–174**, 179 (2000).
15. S. Komazaki, T. Hashida, T. Shoji, and K. Suzuki: Development of small punch tests for creep property measurement of tungsten-alloyed 9% Cr ferritic steels. *J. Test. Eval.* **28**, 249 (2000).
16. H. Kutsumi, A. Chino, and Y. Ishibashi: Quantitative analysis of laves phase and carbide in high Cr heat-resistance ferritic steels. *Tetsu to Hagane* **78**, 594 (1992) in Japanese.
17. R. Ishii, Y. Tsuda, K. Fujiyama, K. Kimura, and K. Saito: Creep damage estimation based on the softening behavior of 10Cr-1Mo-1W-VNbN steel. *Tetsu to Hagane* **89**, 699 (2003) in Japanese.
18. K. Sawada, M. Takeda, K. Maruyama, R. Ishii, M. Yamada, Y. Nagae, and R. Komine: Effect of W on recovery of lath structure during creep of high chromium martensite steels. *Mater. Sci. Eng., A* **267**, 19 (1999).
19. M. Kimura, K. Yamaguchi, M. Hayakawa, and K. Kobayashi: Microstructure and grain boundary precipitates in 9-12% Cr ferritic heat-resisting steels. *Tetsu to Hagane* **90**, 27 (2004) in Japanese.
20. W.D. Nix and H. Gao: Indentation size effects in crystalline materials: A law for strain gradient plasticity. *J. Mech. Phys. Solids* **46**, 411 (1998).
21. H. Gao and Y. Huang: Geometrically necessary dislocation and size-dependent plasticity. *Scripta Mater.* **48**, 113 (2003).
22. K.L. Johnson: The correlation of indentation experiments. *J. Mech. Phys. Solids* **18**, 115 (1970).
23. M. Yamada, O. Watanabe, Y. Yoshioka, and M. Miyazaki: Development of advanced 12Cr steel rotor forgings. *Tetsu to Hagane* **76**, 1084 (1990) in Japanese.